Cross-detector scatter issues in dual synchronous tomography: An affine projection correction protocol

J.M. Létang, Joël Lachambre, Éric Maire

Cross-detector scatter issues in dual synchronous tomography: an affine projection correction protocol

Jean Michel Létang[a,*], Joël Lachambre[b] and Éric Maire[b]

[a]INSA-Lyon, Université Claude Bernard Lyon 1, CNRS, Inserm, CREATIS UMR 5220 U1294, F-69373 Lyon, France
[b]INSA Lyon, Université Claude Bernard Lyon 1, CNRS, MATEIS UMR 5510, F-69621 Villeurbanne, France

ARTICLE INFO

Keywords:
Cone-beam computed tomography
Dual x-ray source
Flat-field correction
Detector scatter

ABSTRACT

Dual-beam x-ray tomography systems are paving the way for new experimental procedures, such as multi-resolution and multi-energy imaging, where synchronous acquisitions are essential. However, in such systems, cross-detector scatter between the detecting devices can occur as the two beamlines operate simultaneously. This paper proposes a new affine image transformation model of each projection to correct for these cross-detector scatter issues. A toy tomography test case is presented to assess the feasibility and performance of the proposed correction method.

1. Introduction

The first micro-CT and dual-source CT imaging systems appeared at the same time in the early 1980s and were mainly laboratory prototypes [13, 6]. Initially, micro-CT has been developed for the examination of the 3D bone architecture [7] and dual-source CT to minimize the acquisition time [14, 15]. The spatial resolution of high-resolution CT systems currently in clinical use is below 0.5 µm (e.g. in dental composites [8]), and the temporal resolution of dual-source CT systems below 70 ms (e.g. in cardiac imaging [18]).

Dual-source clinical systems mostly use linear detectors with translation tables [2], i.e. a fan-beam instead of a cone-beam irradiation geometry, (i) to allow whole-body imaging and (ii) to limit damages caused by scattering [9]. The image degradation caused by the detector self-scatter is also significant in CBCT and can usually be modeled by convolution kernels in the detector point-spread function [4, 3]. Among dual-source cone-beam computed tomography CBCT systems designed for fundamental and engineering studies, it is worth noting the simultaneous neutron and x-ray imaging instrument that has been developed since 2016 at ILL [19]. To reduce the 99.9% of the scattered neutrons, a specific protective layer of boron carbide had to be used.

The development of high-resolution high-energy dual-beam CBCT systems [11] introduces new challenges for quantitative imaging, in particular cross-detector scatter during simultaneous beam-line operation. Artefact reduction procedures for quantitative imaging involve several methods and devices such as flat-field correction and beam filtering [20]. Various adaptations of the conventional flat-field projection correction [16, 12] have been proposed to account for non-linearities in the detector response [10], but the cross-detector scatter that occurs in dual-sources systems has not been addressed yet. The flat-field correction must therefore be revised for dual-beam synchronous CBCT systems.

To derive a new data correction scheme for cross-detector scatter, we first model the image formation of a dual-beamline such as this one designed for example by the MateIS laboratory [11], and we then present the dual-beam correction. We finally evaluate the feasibility and performance of the method using a toy tomography test case acquired at the dual beamline facility.

2. Materials and Methods

The following notations are used throughout the paper:

- $\Phi(p,t)$ refers to a x-ray flux per unit surface,
- $P(p,t)$ refers to a measured x-ray projection,
- $I(p,t)$ refers to an attenuation image after flat-field normalization,

and all these variables are expressed in terms of pixel p and time t.

2.1. Dual-beam fluence model

During CT scans, projections are typically indexed by the rotation angle. However, in dual-beam systems, the beamlines are at different angle values for a specific time, because of the angular shift of approximately $\pi/2$ between them. Therefore, it is more intuitive to parameterize the projections using time t, as there exists a bijection for each beamline between the projection angle and the acquisition time.

Given p the pixel image index and i the beamline index (with $i \in [1,2]$), the fluence components when the beamline i is operated alone (i.e. single-beam mode) are given by:

- Direct transmitted fluence $\phi_i(p,t)$, i.e. with object sample but without scatter,
- Object scatter fluence $\phi^s_{i\leftarrow i}(p,t)$ from beam source i to detector i,

*Corresponding author
jean.letang@creatis.insa-lyon.fr (J.M. Létang); eric.maire@insa-lyon.fr (É. Maire)
ORCID(s): 0000-0003-2583-782X (J.M. Létang); 0000-0001-8550-5187 (É. Maire)

which gives the following observed fluence impinging upon detector i:

$$\phi_i^o(p,t) = \phi_i(p,t) + \phi_{i\leftarrow i}^s(p,t). \quad (1)$$

When tube 2 is also in operation, the radiation from tube 2 causes two additional components for the detector 1: detector scatter $\phi_{1\leftarrow 2}^d(p,t)$ and object scatter $\phi_{1\leftarrow 2}^s(p,t)$. In dual-beam mode, the total fluence for the detector 1 is therefore:

$$\phi_1^x(p,t) = \phi_1^o(p,t) + \phi_{1\leftarrow 2}^s(p,t) + \phi_{1\leftarrow 2}^d(p,t) \quad (2)$$

where exponent 'x' stands for "cross" (ie both tubes are in operation). The dual beamline setup and the notation for the fluence components are summarized in Figure 1.

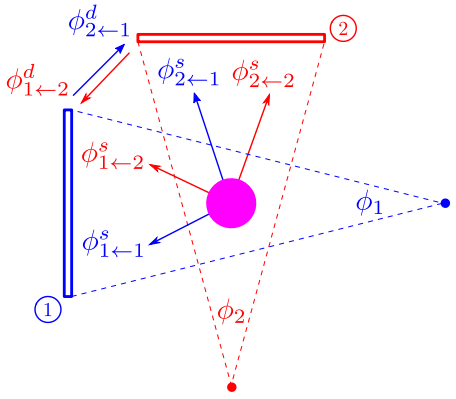

Figure 1: Dual beamline setup and x-ray fluence components.

The cross-detector scatter $\phi_{1\leftarrow 2}^d(p,t)$ in Equation 2 cannot be measured on-line since both tubes are in operation, but it can be estimated off-line. During the flat-field acquisition procedure, we just need to add the cross-detector scatter measurement and we get for beamline 1:

- Full field fluence $\phi_1^*(p)$ without object,
- The cross-detector scatter $\phi_{1\leftarrow 2}^{d*}(p)$ to detector 1 using tube 2 alone and without object,

where exponent '*' is used in the notations to specify when the acquisition is without object. From this off-line measurement of the cross-detector scatter in single-beam mode, the cross-detector scatter at a specific time t during the sinogram acquisition in dual-beam mode can be approximated using a linear scaling by the mean intensity of the total fluence of detector 2 at that same time t as follows:

$$\phi_{1\leftarrow 2}^d(p,t) = \frac{\langle \phi_2^x \rangle(t)}{\langle \phi_2^* \rangle} \phi_{1\leftarrow 2}^{d*}(p). \quad (3)$$

with $\langle\rangle$ stands for the mean over all pixels p.

In conventional tomography setups, there is a certain distance between the sample and the detector (the so-called "air gap"). In microtomography, large magnifications are usually used and the sample is even be closer to the source than the detector. Boellaard et al [5] showed that the scattered dose profile becomes rapidly flat when the air gap is increased. The postulate that object scatter has a very low spatial frequency distribution at the level of the detector is therefore fair in microtomography setups, and it can be approximated constant on the detector 1:

$$\phi_{1\leftarrow 1}^s(p,t) + \phi_{1\leftarrow 2}^s(p,t) = \phi_1^s(p,t) \simeq \langle \phi_1^s \rangle(t). \quad (4)$$

Equation 4 shows that there are two superimposed contributions to the object scatter in dual-beam mode for a given beamline detector, as the object is irradiated by both x-ray tubes.

Using Equations 4 and 3, the image formation model described by Equation 2 becomes:

$$\phi_1^x(p,t) = \phi_1(p,t) + \langle \phi_1^s \rangle(t) + \frac{\langle \phi_2^x \rangle(t)}{\langle \phi_2^* \rangle} \phi_{1\leftarrow 2}^{d*}(p) \quad (5)$$

2.2. Dual-beam correction

Introducing now the detector responses $D_i(p)$ – assumed time, energy and direction invariant – the detector acquisition model may be written as

$$P_i(p,t) = D_i(p)\ \phi_i(p,t) \quad (6)$$

when the detector offset (dark current) is already corrected for. The conventional flat-field correction to compute the attenuation image I_i from projection P_i is:

$$I_i(p,t) = \frac{P_i(p,t)}{P_i^*(p,t)} \quad (7)$$

which is just a pixel-wise gain normalization of offset-corrected projections.

Applying now this gain normalization to Equation 5, the image formation model then becomes for beamline 1

$$I_1^x(p,t) = I_1(p,t) + \langle I_1^s \rangle(t) + \langle I_2^x \rangle(t)\ I_{1\leftarrow 2}^{d*}(p). \quad (8)$$

where $\langle I_1^s \rangle(t)$ and $\langle I_2^x \rangle(t)$ are image constants for a specific time t (i.e. not pixel dependent).

The image formation model for beamline 1 given in equation 8 is therefore an affine perturbation at a given time t of the direct transmitted image $I_1(p,t)$ by the cross-detector scatter $I_{1\leftarrow 2}^{d*}(p)$ (acquired off-line),

$$I_1^x(p,t) = I_1(p,t) + \left[A_1(t) + B_1(t)\, I_{1\leftarrow 2}^{d*}(p)\right] \quad (9)$$

where $A_1(t)$ accounts for the object scatter and $B_1(t)$ for the cross-detector scatter weight. We can thus have the following expression of a dual-beam correction protocol

$$I_1(p,t) = I_1^x(p,t) - \left[A_1(t) + B_1(t)\, I_{1\leftarrow 2}^{d*}(p)\right]. \quad (10)$$

We propose here a very simple procedure for the flat-field correction in dual mode. It only requires to adjust $A_1(t)$ and $B_1(t)$ to make sure that $I_1(p,t) = 1$ in the air regions of the attenuation image. Equation 10 could be written for beamline 2 in a similar way. Table 1 summarizes the protocol required for our correction protocol.

Table 1
Cross-detector scatter correction protocol

1. Data acquisition without object in single-beam mode,
   (a) $P_1^*(p)$, the detector 1 acquisition with beam 1,
   (b) $P_{1\leftarrow 2}^{d*}(p)$, the detector 1 acquisition with beam 2,
   (c) $P_2^*(p)$, the detector 2 acquisition with beam 2,
   (d) $P_{2\leftarrow 1}^{d*}(p)$, the detector 2 acquisition with beam 1,
2. Data acquisition with object in dual-beam mode,
   (a) $P_1^x(p,t)$, the sinogram of beamline 1,
   (b) $P_2^x(p,t)$, the sinogram of beamline 2.
3. For beamline 1 and for each projection $I_1^x(p,t)$:
   (a) Compute the gain-normalized images with single-beam data
   $$I_1^x(p,t) = \frac{P_1^x(p,t)}{P_1^*(p)} \text{ and } I_{1\leftarrow 2}^{d*}(p) = \frac{P_{1\leftarrow 2}^{d*}(p)}{P_1^*(p)}$$
   (b) Compute the mean value in two air-only ROIs in the projection, one on the left ($k = L$) and one on the right ($k = R$) since the intensity gradient of the cross-detector scatter is horizontal
   $$m_{k1}(t) = \left\langle I_1^x(p,t) \right\rangle_{\text{ROI}_{k1}}$$
   (c) For the same two ROIs ($k \in [L,R]$) in the cross-detector scatter calibration image, compute the two corresponding mean values
   $$s_{k1} = \left\langle I_{1\leftarrow 2}^{d*}(p) \right\rangle_{\text{ROI}_{k1}}$$
   (d) Compute the linear affine correction coefficients
   $$A_1(t) = \left[\frac{m_{L1}(t)\, s_{R1} - m_{R1}(t)\, s_{L1}}{s_{R1} - s_{L1}}\right] - 1$$
   and
   $$B_1(t) = \frac{m_{R1}(t) - m_{L1}(t)}{s_{R1} - s_{L1}}$$
   (e) Apply equation 10 to compute $I_1(p,t)$.
4. Repeat steps (a) to (e) for beamline 2 and for each projection $I_2^x(p,t)$.

2.3. Toy test-case

In order to validate the proposed flat-field correction protocol, the following dual-beam setup has been used. For both x-ray tubes, high voltage was set to 200 kV, current was to to 100 µA, and a 1 mm copper additional filtration was used. The flat panel resolutions were 2872×2872 squared pixels of 150 µm side. For beamline 1 (resp. 2), the source-to-detector distance was 746 mm (resp. 749 mm), and the source-to-isocenter distance 185 mm (resp. 187 mm).

The object was a cube (4 cm side) made of an aluminium alloy. For the tomography scan, 1216 projections over 2π were taken. A picture of the setup is shown in Figure 2. The standard FDK reconstruction algorithm from the ASTRA toolbox [1] was used. No post-processing has been used to correct for beam-hardening or ring artefacts.

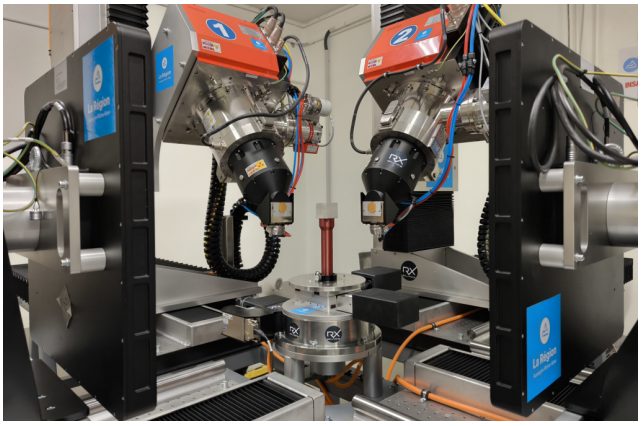

Figure 2: Picture of the toy test-case: the dual beamline with the aluminium cube.

To test the proposed dual-beam correction, the following projections are acquired:

- $P_1^*(p)$ is the detector 1 acquisition with tube 1 alone and no object,
- $P_{1\leftarrow 2}^{d*}(p)$ is the detector 1 acquisition with tube 2 alone and no object,
- $P_1^x(p,t)$ is the sinogram acquisition sequence by detector 1 with the aluminium cube and both tubes in operation,

and the following projections for benchmarking purposes (see next section):

- $P_1^o(p,t)$ is the sinogram acquisition sequence by detector 1 with tube 1 alone, this is for the reference method (a),
- $P_1^{x*}(p)$ is the detector 1 acquisition with both tubes in operation and no object, this is for the method (d).

3. Benchmarking protocol

Three different corrections methods are benchmarked and compared to the reference:

(SB) the reference **S**ingle-**B**eam mode acquisition with the conventional flat-field correction (Equation 7),

(DB-DBC) the **D**ual-**B**eam mode acquisition with the proposed **D**ual-**B**eam **C**orrection (Equation 10),

(DB-SBF) the **D**ual-**B**eam mode acquisition with the conventional **S**ingle-**B**eam **F**lat-field method (Equation 7),

(DB-DBF) the **D**ual-**B**eam mode acquisition with a **D**ual-**B**eam **F**lat-field method using the full field projection in dual-beam mode $P_i^{x*}(p)$ instead of the full-field projection in single-beam mode $P_i^*(p)$ in Equation 7.

The labels SB, DB-DBC, DB-SBF and DB-DBF will be used hereafter to refer to each correction method.

4. Results

The cross-detector scatter $I^{d*}_{2\leftarrow 1}(p)$ for beamline 2 originating from beamline 1 is shown in Figure 3. The cross-detector scatter is almost constant vertically and exhibits an horizontal increase which reaches close to 7% of the white image. The brighter part of this image is on the left-hand side, as expected from the setup shown in Figure 1.

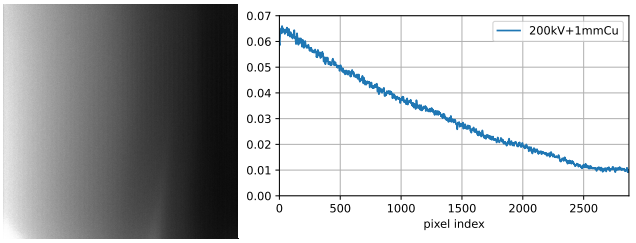

Figure 3: Cross-detector scatter $I^{d*}_{2\leftarrow 1}(p)$ (left) and central horizontal profile (right). The profile intensity value is the fraction of the projection without object $P^*_i(p,t)$.

An estimation of the object scatter can be obtained by subtracting the cross-detector scatter with and without the aluminium cube in the sample holder, namely $I^{d}_{1\leftarrow 2}(p,t) - I^{d*}_{1\leftarrow 2}(p)$. Figure 4 shows the two cross-scatter images measured by detector 1, and their difference. While the mean value of the cross-detector scatter image is about 3%, as expected from Figure 3, the mean value of the detector scatter image is ten-times smaller and almost flat.

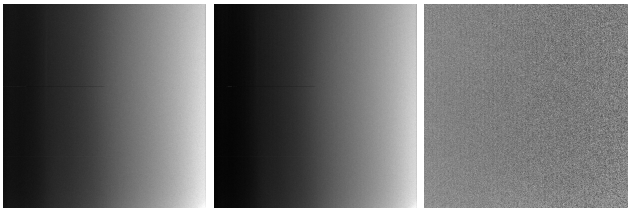

Figure 4: Object scatter. Left: object and cross-detector scatter $I^{d}_{1\leftarrow 2}(p,950)$ in a single beam acquisition (image average: 3.01%). Middle: cross-detector scatter image $I^{d*}_{1\leftarrow 2}(p)$ without sample (image average: 2.77%). Right: object scatter image computed by the difference between the two (image average: 0.24%).

A projection of the aluminium-alloy cube at $t = 950$ (a.u.) for the beamline 1 with dual-beam mode is shown in Figure 5 (left figure). The figure also shows a line profile of intensity (right figure). An horizontal drift of the pixel values is visible in the line profile, in accordance with the cross-detector scatter coming from beamline 2 shown in Figure 3.

The proposed dual-beam correction method has been applied to projection $t = 950$. Figure 6 shows the difference image with respect to the reference single-beam acquisition method SB. The overall error is about 10^{-3} and constant in the image without visible object structure. The conventional flat-field method DB-SBF with a single-beam white image fails at correcting the cross-detector scatter drift in the image as figure 7-left shows: the error is about a few percents. The

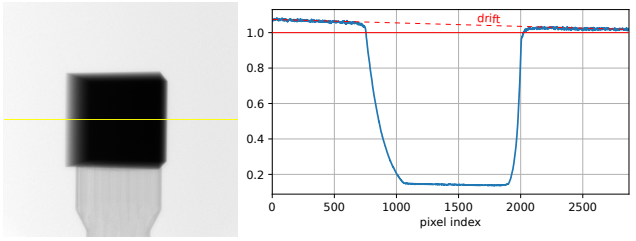

Figure 5: Projection of the aluminium cube $I^{x}_{2}(p,950)$ (left) and central horizontal profile (right). The profile intensity value is the fraction of the projection without object $P^*_i(p,t)$.

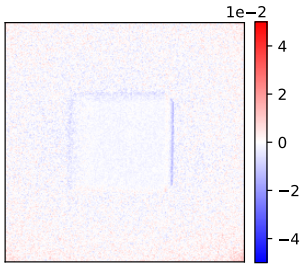

Figure 6: Difference image between the proposed dual-beam correction method DB-MDC and the reference single-beam acquisition method SB. Projection at $t = 950$ is shown.

flat-field method DB-DBF with a dual-beam white image displayed in figure 7-right corrects the cross-detector scatter (the error is indeed close to 0 in air regions) but corrupts the object attenuation by a few percents.

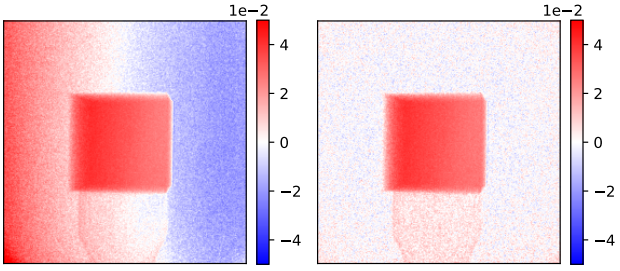

Figure 7: Left: Difference image between the conventional single-beam correction method DB-SBF and the reference single-beam acquisition method SB. Right: Difference image between the dual-beam correction method DB-DBF and the reference single-beam acquisition method SB. Projections at $t = 950$ are shown.

The same reconstructed CT slice 608 is displayed in figure 8 for the four benchmarked methods: the reference single-beam CT acquisition SB and three dual-beam CT acquisition with the proposed correction DB-DBC, the conventional single-beam normalization DB-SBF, and the dual-beam gain normalization DB-DBF. The proposed dual-beam correction method (b) succeeds in recovering quantitatively the linear attenuation coefficient reconstructed by the reference method SB.

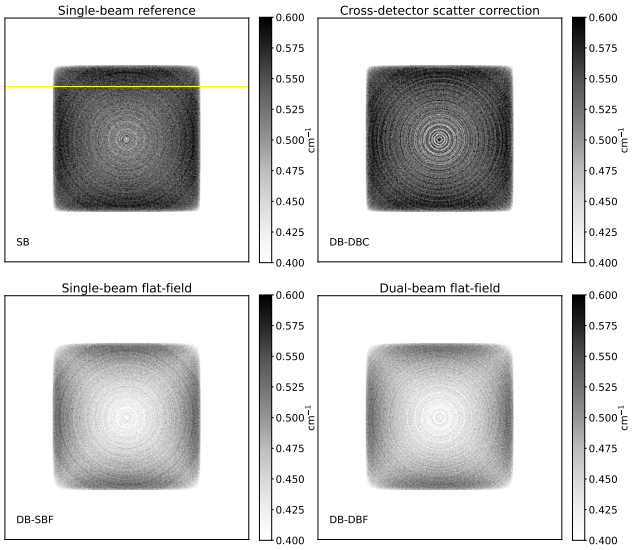

Figure 8: Slice 608 of the aluminium cube. From top to bottom and from left to right: reference CT acquisition in single-beam CT mode SB, then in dual-beam CT mode, the proposed dual-beam cross-detector scatter correction DB-DBC, the conventional single-beam flat-field DB-SBF, and the dual-beam flat-field DB-DBF. The LUT contrast (units are in cm^{-1}) is the same for all images.

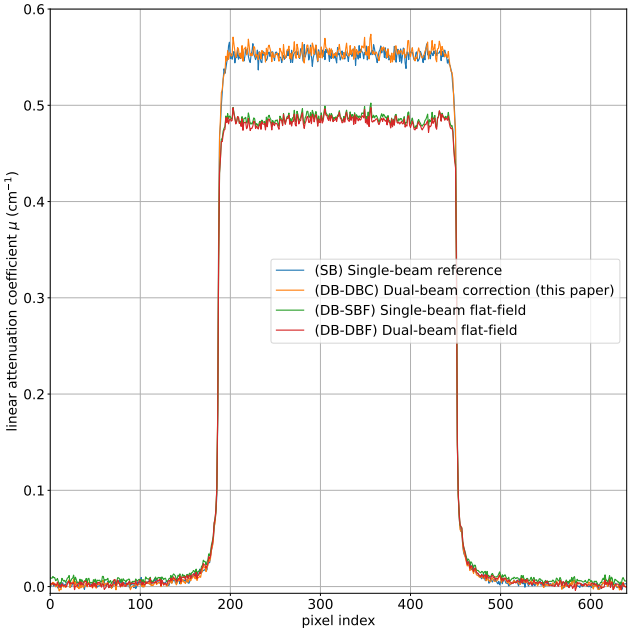

Figure 9: Profiles sampled in slice 608 of the four benchmarked methods shown in Figure 8. The profile location is the yellow line in that referenced figure.

This is also clearly visible in the intensity profiles that have been sampled in the four slices, the location of the profile is shown as the yellow line in the reference single-beam CT slice (top left of Figure 8). Those four profiles are depicted in Figure 9. Both benchmarking methods DB-SBF and DB-DBF suffer a contrast reduction of more than 12% in the reconstructed linear attenuation coefficient values. The mean energy of a 200 kV x-ray beam with a 1 mm additional copper filtration is about 100 keV, and the linear attenuation coefficient of the aluminium alloy at this energy is about 0.56 cm^{-1}, which is in line with the reconstructed values in the reference image (see Figures 8 and 9).

5. Discussion

The reconstruction slices in Figure 8 and the corresponding profiles in Figure 9 show that the proposed correction compensates for the disturbances caused by the cross-detector scatter. On the contrary, the positive transmission bias, that was still visible in projection 950 after both single-beam and dual-beam gain normalizations (see Figure 7), induces an under-estimation of the reconstructed linear attenuation coefficient as Figure 9 shows. The remaining reconstructed discrepancy is negligible but the proposed cross-detector scatter correction method does not reduce the magnitude of the beam-hardening artifacts which is about the same (cupping effects visible in Figure 8). The toy test-case validated the proposed correction method, but samples with very pronounced spatial structures that vary greatly from one projection to another could generate cross-detector scatter images with variable spatial distributions during rotation of the dual tomo scan, deviating from the reference cross-detector scatter distribution without sample. The approximation of equation 3 would then no longer be valid, and these situations will have to be studied in greater detail.

The proposed cross-detector scatter correction protocol compensates for object scatter, but assumes a constant scatter image (see equation 4): any deviation from this constant approximation might infer a contrast reduction in the images. However, the Monte Carlo study of Sisniega et al [17] related to CBCT scatter distributions showed (i) that incoherent (Compton) scattering has a very low frequency structural information, and (ii) that contrast reduction due to patient scatter is highly dependent on the CBCT configuration (organ size and geometry). The imaging samples in microtomography setups are usually much smaller than the detector size and the distance between the sample and the detector is large: we observed in the toy test-case that the object scatter was an order of magnitude smaller than cross-detector scatter, which induced a reduction in contrast of about 12% in the reconstructed images (see new Figures 4 and 9). Therefore, the contrast reduction caused by the residual structural information of the object scatter after the proposed correction protocol is likely to be negligible.

It is worth noting that the setups of beamlines 1 and 2 may be different in terms of magnification, region of interest, voltage and intensity: the proposed dual-beam correction makes no assumption in this regard as long as air-regions are present to fit the two parameters of the affine correction model in equation 10.

6. Conclusion

We presented a new scheme for cross-detector scatter correction during the flat-field normalization in dual-beam mode CT acquisitions. Conventional flat-field gain normalizations are not able to correctly recover the induced bias, contrarily to the proposed additional correction.

Declaration of Competing Interest

The authors declare that they have no known competing financial interests or personal relationships that could have appeared to influence the work reported in this paper.

Acknowledgments

The DTHE new device described in this paper was co-funded by the French Region AURA (IRICE project 2022) by INSA-Lyon (INSA equipex project 2022) by CNRS and by Institut Carnot Ingenierie at Lyon.

References

[1] van Aarle, W., Palenstijn, W.J., Cant, J., Janssens, E., Bleichrodt, F., Dabravolski, A., De Beenhouwer, J., Batenburg, K.J., Sijbers, J., 2016. Fast and flexible x-ray tomography using the ASTRA toolbox. Optics express 24, 25129–25147. doi:10.1364/OE.24.025129.

[2] Baldi, D., Tramontano, L., Alfano, V., Punzo, B., Cavaliere, C., Salvatore, M., 2020. Whole body low dose computed tomography using third-generation dual-source multidetector with spectral shaping: Protocol optimization and literature review. Dose-Response 18, 155932582097313. doi:10.1177/1559325820973131.

[3] Bhatia, N., Tisseur, D., Létang, J.M., 2017. Convolution-based scatter correction using kernels combining measurements and monte carlo simulations. Journal of X-Ray Science and Technology 25, 613–628. doi:10.3233/XST-16185.

[4] Bhatia, N., Tisseur, D., Valton, S., Létang, J.M., 2016. Separable scatter model of the detector and object contributions using continuously thickness-adapted kernels in CBCT. Journal of X-Ray Science and Technology 24, 723–732. URL: http://doi.org/10.3233/XST-160583, doi:10.3233/XST-160583.

[5] Boellaard, R., van Herk, M., Mijnheer, B.J., 1997. A convolution model to convert transmission dose images to exit dose distributions. Med Phys 24, 189–199.

[6] Eidelman, S.I., Shwartz, B.A., 2012. Handbook of Particle Detection and Imaging. 1 ed., Springer-Verlag Berlin Heidelberg.

[7] Feldkamp, L.A., Goldstein, S.A., Parfitt, M.A., Jesion, G., Kleerekoper, M., 1989. The direct examination of three-dimensional bone architecture in vitro by computed tomography. Journal of Bone and Mineral Research 4, 3–11. doi:10.1002/jbmr.5650040103.

[8] Haugen, H.J., Qasim, S.B., Matinlinna, J.P., Vallittu, P., Nogueira, L.P., 2020. Nano-CT as tool for characterization of dental resin composites. Scientific Reports 10. doi:10.1038/s41598-020-72599-y.

[9] Jarry, G., Graham, S.A., Moseley, D.J., Jaffray, D.J., Siewerdsen, J.H., Verhaegen, F., 2006. Characterization of scattered radiation in kV CBCT images using Monte Carlo simulations. Medical Physics 33, 4320–4329. doi:10.1118/1.2358324.

[10] Kwan, A.L.C., Seibert, J.A., Boone, J.M., 2006. An improved method for flat-field correction of flat panel x-ray detector. Medical Physics 33, 391. URL: 10.1118/1.2163388, doi:10.1118/1.2163388.

[11] Maire, E., Bonnard, G., Adrien, J., Boulnat, X., Létang, J.M., Lachambre, J., 2024. Dual beam microfocus high-energy tomography: Towards multimodal and faster laboratory experiments. Tomography of Materials and Structures 5, 100030. doi:10.1016/j.tmater.2024.100030.

[12] Moy, J.P., Bosset, B., 1999. How does real offset and gain correction affect the DQE in images from x-ray flat detectors?, in: Boone, J.M., Dobbins III, J.T. (Eds.), SPIE Proceedings, SPIE. pp. 90–97. doi:10.1117/12.349555.

[13] Ritman, E.L., 2011. Current status of developments and applications of micro-CT. Annual Review of Biomedical Engineering 13, 531–552. doi:10.1146/annurev-bioeng-071910-124717.

[14] Ritman, E.L., Kinsey, J.H., Robb, R.A., Harris, L.D., Gilbert, B.K., 1980. Physics and technical considerations in the design of the DSR: a high temporal resolution volume scanner. American Journal of Roentgenology 134, 369–374. doi:10.2214/ajr.134.2.369.

[15] Saint-Felix, D., Trousset, Y., Picard, C., Ponchut, C., Romeas, R., Rougee, A., 1994. In vivo evaluation of a new system for 3D computerized angiography. Physics in Medicine and Biology 39, 583–595. doi:10.1088/0031-9155/39/3/020.

[16] Seibert, J.A., Boone, J.M., Lindfors, K.K., 1998. Flat-field correction technique for digital detectors, in: Dobbins III, J.T., Boone, J.M. (Eds.), Medical Imaging 1998: Physics of Medical Imaging, SPIE. pp. 348–354. doi:10.1117/12.317034.

[17] Sisniega, A., Zbijewski, W., Badal, A., Kyprianou, I.S., Stayman, J.W., Vaquero, J.J., Siewerdsen, J.H., 2013. Monte carlo study of the effects of system geometry and antiscatter grids on cone-beam CT scatter distributions. Medical physics 40, 051915. doi:10.1118/1.4801895.

[18] Soschynski, M., Hagen, F., Baumann, S., Hagar, M.T., Weiss, J., Krauss, T., Schlett, C.L., von zur Mühlen, C., Bamberg, F., Nikolaou, K., Greulich, S., Froelich, M.F., Riffel, P., Overhoff, D., Papavassiliu, T., Schoenberg, S.O., Faby, S., Ulzheimer, S., Ayx, I., Krumm, P., 2022. High temporal resolution dual-source photon-counting CT for coronary artery disease: Initial multicenter clinical experience. Journal of Clinical Medicine 11, 6003. doi:10.3390/jcm11206003.

[19] Tengattini, A., Lenoir, N., Andò, E., Giroud, B., Atkins, D., Beaucour, J., Viggiani, G., 2020. NeXT-Grenoble, the neutron and x-ray tomograph in Grenoble. Nuclear Instruments and Methods in Physics Research Section A: Accelerators, Spectrometers, Detectors and Associated Equipment 968, 163939. doi:10.1016/j.nima.2020.163939.

[20] Withers, P.J., Bouman, C., Carmignato, S., Cnudde, V., Grimaldi, D., Hagen, C.K., Maire, E., Manley, M., Du Plessis, A., Stock, S.R., 2021. X-ray computed tomography. Nature Reviews Methods Primers 1. doi:10.1038/s43586-021-00015-4.